



HAL
open science

Spectral endmember variability on hyperspectral datasets of a Martian meteorite - Implications for planetary surfaces

Lu Pan, Cathy Quantin-Nataf, Lucia Mandon, Mélissa Martinot, Pierre Beck

► **To cite this version:**

Lu Pan, Cathy Quantin-Nataf, Lucia Mandon, Mélissa Martinot, Pierre Beck. Spectral endmember variability on hyperspectral datasets of a Martian meteorite - Implications for planetary surfaces. *Icarus*, 2021, 370, 10.1016/j.icarus.2021.114656 . insu-03705257

HAL Id: insu-03705257

<https://insu.hal.science/insu-03705257v1>

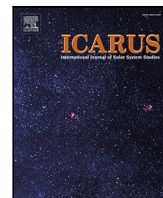
Submitted on 27 Jun 2022

HAL is a multi-disciplinary open access archive for the deposit and dissemination of scientific research documents, whether they are published or not. The documents may come from teaching and research institutions in France or abroad, or from public or private research centers.

L'archive ouverte pluridisciplinaire **HAL**, est destinée au dépôt et à la diffusion de documents scientifiques de niveau recherche, publiés ou non, émanant des établissements d'enseignement et de recherche français ou étrangers, des laboratoires publics ou privés.



Distributed under a Creative Commons Attribution 4.0 International License



Research Paper

Spectral endmember variability on hyperspectral datasets of a martian meteorite — implications for planetary surfaces

Lu Pan^{a,b,*}, Cathy Quantin-Nataf^a, Lucia Mandon^{a,c}, Mélissa Martinot^{a,d}, Pierre Beck^e^a University of Lyon, University Lyon 1, ENS de Lyon, CNRS, LGL-TPE, F-69622, Villeurbanne, 69222, France^b University of Copenhagen, GLOBE institute, Center for Star and Planet Formation, Denmark^c LESIA, Observatoire de Paris, Université PSL, CNRS, Sorbonne Université, Université de Paris, 5 place Janssen, 92195 Meudon, France^d University of Central Florida, Department of Physics, United States of America^e Université Grenoble Alpes, CNRS, Institut de Planétologie et d'Astrophysique de Grenoble (IPAG), UMR 5274, Grenoble F-38041, France

ARTICLE INFO

Keywords:

Spectroscopy
Mars, Surface
Meteorites

ABSTRACT

Visible-near-infrared reflectance spectra reveal clues about the mineralogy and composition of planetary surfaces. In most cases, light interacts with a mixture of various components on planetary surfaces. While radiative transfer models have been developed to simulate mixture in particulate surfaces, the extent to which spectral features represent the bulk composition of rock remains unclear. In this study, we present the analysis of a new dataset with hyperspectral imaging of rock slabs at different resolutions to characterize the scaling of spectral data. We address the problem of spectral mixing with high-resolution imaging of Martian meteorite NWA480 at a microscopic scale. The linear combination of each pixel provide an approximate to the rock's bulk spectra. However, we find the impurities, fractures and zoning create wide spectral variability in the mineral crystals. In addition, the widespread opaque minerals may also darken the spectra, resulting in non-unique interpretation of the bulk spectra. These complexities in the natural samples prevent an accurate mineral abundance retrieval using unmixing algorithms with select spectral endmembers. We suggest applying recently developed algorithms on unmixing with spectral variability with the consideration of the petrologic context would be necessary to improve the quantitative analysis of planetary surfaces.

1. Introduction

Visible and shortwave near-infrared hyperspectral reflectance spectra of a planetary surface provide compositional information that improves our understanding of geological processes, including planetary evolution and water–rock interaction (Adams, 1974; Clark et al., 1990; Fischer and Pieters, 1994; Tompkins and Pieters, 1999; Bibring et al., 2006; Murchie et al., 2009; Kokaly et al., 2017). Enormous amounts of efforts have been put into the characterization of the spectra of mineral separates, producing a large set of spectral libraries (e.g., the United States Geological Survey (USGS) Spectral Library 07 (Clark et al., 1990; Kokaly et al., 2017), NASA Reflectance Experiment Laboratory (RELAB) Facility (Pieters, 1983), the RRUFF spectral libraries (Lafuente et al., 2015)) where the visible-near-infrared spectra of most common minerals have been measured and archived. These minerals' typical spectral absorption features have been used to identify mineralogy on planetary surfaces as “fingerprints”. In contrast, quantitative understanding of planetary bodies through reflectance spectroscopy is more difficult.

Various approaches based on radiative transfer models (Hapke and Wells, 1981; Hapke, 1981, 1984; Shkuratov et al., 1999) have been developed to characterize particulate surfaces, assuming closely packed pure mineral grains. Such models typically require input of various physical parameters that describe the minerals' interaction with light, including the optical constants, phase function, back scattering and macroscale roughness. Spectral datasets acquired in the lab have been analyzed to investigate the physical meaning of these parameters (Cord et al., 2003; Mustard and Pieters, 1989; Li and Milliken, 2015). The inversion of binary spectral mixtures of lunar analog materials and meteorites measured in laboratory has shown that radiative transfer models can provide abundance estimates within 5% of minerals with known spectral properties *a priori* and controlled grain size (Mustard and Pieters, 1989; Li and Milliken, 2015; Harris and Grindrod, 2018; Yang et al., 2019). As the underlying assumption dictates, the modal abundance prediction based on spectral data provides better results for

* Correspondence to: Center for Star and Planet Formation, GLOBE Institute, Øster Voldgade 5-7, København, 1350, Denmark.
E-mail address: lu.pan@sund.ku.dk (L. Pan).

<https://doi.org/10.1016/j.icarus.2021.114656>

Received 30 April 2021; Received in revised form 24 July 2021; Accepted 10 August 2021

Available online 18 August 2021

0019-1035/© 2021 The Author(s). Published by Elsevier Inc. This is an open access article under the CC BY license (<http://creativecommons.org/licenses/by/4.0/>).

rock powder than rock chips in the analysis for Howadite, Eucrite and Diogenite (HED) meteorite samples (Li and Milliken, 2015).

Meanwhile, rock outcrops are essential targets for planetary exploration as direct records of the petrogenesis and register a given location's geologic context. The study of rock outcrops can provide a constrained solution to the temperature, pressure, and water solution, the water activity and pH of the environment in which the mineralogical species formed, a common practice in terrestrial geology. New datasets acquired by hyperspectral or multispectral cameras from a distance to the target (several meters and from orbit) is complicated by the spectral mixing of minerals in a rock at the micrometer scale. Previous studies have shown that rocks with similar bulk composition, but a different texture, can have significantly varying spectral patterns in the bulk spectra (Crowley, 1986; Harloff and Arnold, 2001; Pompilio et al., 2007; Carli et al., 2014). The fact that spectral endmember components in a rock are not equivalent to the mineral separates from the same rock also complicates the understanding of mineral unmixing, as shown by the study of returned samples from the Apollo mission during the Lunar Rock and Mineral Characterization Consortium (LRMCC) (Isaacson et al., 2011). Additionally, a dark, fine-grained matrix component is considered to dominate bulk spectra in intimate mixing models. In contrast, the large phenocrysts often dominate the bulk rock spectra, presenting an obvious paradox (Carli et al., 2014, 2015). These previous studies using spectrometer data point out that instead of taking previous radiative transfer mixing models that deal with particulate mixtures, new approaches need to be developed to understand spectra taken on rock chip's surfaces quantitatively.

Hyperspectral cameras can resolve micro-scale heterogeneities while retrieving spectral data. The high-resolution hyperspectral images provide a new tool to address this question of unmixing within bulk rock samples. Therefore, hyperspectral cameras have been used to characterize the mineralogy of rock samples in laboratory measurements and outcrop measurements in the field (Greenberger et al., 2015, 2020), and widely applied for biomedical (Lu and Fei, 2014; Johnson et al., 2007; Vo-Dinh, 2004) and industrial applications (Gowen et al., 2015; Tatzer et al., 2005; Feng and Sun, 2012). In this study, we present new datasets using laboratory measurements from a hyperspectral imaging spectrometer on a Martian meteorite to bring novel lights to the controlling factors in spectral endmember variability for unmixing problems in geological applications meteorite at various scales. By obtaining spectral images at various distances and resolutions, we provide a "ground truth" for a hyperspectral image from the micrometer to the millimeter scale. We analyzed bulk spectra and performed classification and linear spectral unmixing on data obtained in the laboratory to validate and discuss the physical and chemical factors affecting spectral properties. Our analysis sheds new light on how mixing occurs at varying resolutions and the major causes for spectral variability. We also discuss the uncertainties in quantitative analysis of short-wavelength infrared spectral datasets and the implications for planetary exploration.

2. Method

2.1. Sample and data acquisition

The Martian meteorite Northwest Africa 480 (NWA 480) was chosen as the sample under investigation, due to its relative high reflectance compared to other Martian meteorites and relevance for igneous petrology on terrestrial planets. NWA 480 is a basaltic shergottite with large pyroxene crystals (up to 1–1.5 mm) in a dark matrix. Previous petrologic investigations (Barrat et al., 2002) showed the mineral composition is 72 volume percent (vol%) zoned pyroxene, 25 vol% maskelynite (shocked amorphous glass with plagioclase composition), 1 vol% opaque minerals and sulfide, 1 vol% phosphate, 1 vol% other minerals including fayalite and silica. The pyroxenes show significant zonations with a low-calcium, magnesium-rich core, an augite rim, and

a Fe-pigeonite outer rim, with variations in major element composition, e.g., the Mg/Ca ratio varies from ~ 20 in the core, to ~ 1 in the augite rim and to ~ 0.1 in the outer rim based on the major element composition reported by Barrat et al. (2002). Li-isotopic ratios of the pyroxene phenocrysts suggest evolving magma composition and possible degassing during the crystallization of the meteorite (Barrat et al., 2002; Beck et al., 2004; Marty et al., 2001). The typical porphyritic structure with pyroxene phenocrysts and dark matrix makes NWA 480 an ideal candidate to investigate mixing effect in igneous rocks.

We acquired hyperspectral data using a HySpex SWIR-384 imaging spectrometer. The cut surface of the sample was placed at the same elevation as the 50% Spectralon[®] calibration target. The samples were illuminated with a 400 to 2500 nm broadband halogen light source at an incidence angle of $\sim 30^\circ$. The sample and calibration target were translated beneath the detector while the detector recorded radiance from the target with line-by-line scanning at nadir position, with an emergence angle of 0° . The data were acquired with wavelength between 930–2500 nm and a spectral sampling of 5.45 nm. The acquisition frame rate and integration time is optimized to reduce saturation and increase contrast. We varied the distance and lenses on the detector so that focused data acquisition would be possible at ~ 2 cm, ~ 30 cm and ~ 1 m, in order to achieve hyperspectral image acquisitions with different resolutions: ~ 50 $\mu\text{m}/\text{pixel}$, ~ 0.2 mm/pixel and ~ 0.7 mm/pixel. Below, we refer to the three images as the "high-resolution" (~ 50 $\mu\text{m}/\text{pixel}$), "medium-resolution" (~ 0.2 mm/pixel) and "low-resolution" (~ 0.7 mm/pixel) images taken at standoff distances of 2 cm, 30 cm, 1 m, respectively.

2.2. Image processing, endmember extraction and unmixing

Here we discuss in detail the method applied here in terms of image processing, endmember selection and unmixing. A simplified workflow of the process is depicted in Fig. 1. Spectral data with the raw Digital Number (DN) were acquired with the calibration target and the sample in the same scene to ensure the same illumination condition for calibration. Dark current was measured before the scan and subtracted. Then the reflectance was calculated using the average of 100–300 pixels of the reflectance target for each column. The three images were masked to the extent of the meteorite surface, and the medium- and low-resolution images were registered to the high-resolution image using manually picked reference points. The images are warped and re-sampled using the nearest neighbor algorithm and therefore only geometrical transformation is made and there is no interpolation in the spectral domain. The image registration is only spatially accurate at the pixel level of the coarser resolution images (0.2, 0.7 mm/pixel) due to the resolution limit. Pixels on the rim of the meteorite showed spectral features that match organic contamination due to a sample holder made of cardboard. In the hyperspectral cube, these pixels were removed automatically using a linear deconvolution and threshold method to identify and select the pixels dominated by the organic endmember. We used the high-resolution image to select the appropriate endmembers for spectral unmixing so that the spectral endmembers well represented the mineralogy of the rock slab at the given resolution. Both supervised and unsupervised methods were used to select the appropriate spectral endmembers.

We manually selected three by three pixel-average spectra of mineral phases identifiable in the supervised classification method through visual investigation. Different types of pyroxenes (low-calcium pyroxene or LCP, high-calcium pyroxene or HCP, dark high-calcium pyroxene, or Dark HCP) could be spectrally differentiated. However, mineralogy in the dark matrix which might include maskelynite, ilmenite, chromite, sulfides, phosphate and other minerals, could not be differentiated due to the lack of spectral features, limited signal-to-noise ratio, and spatial resolution. Therefore, we denoted a "Dark" endmember that is of minimal contribution in reflectance. The "Bright" endmember can be a mineral grain with strong specular reflection and

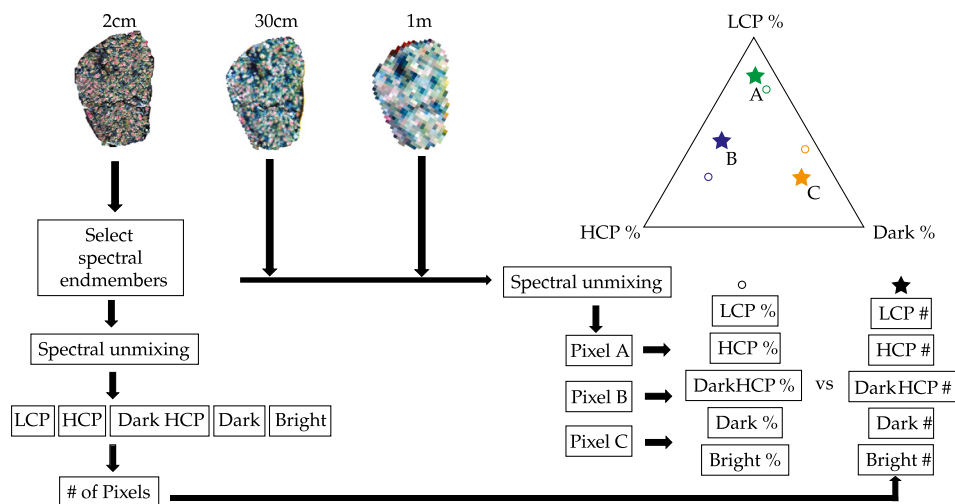


Fig. 1. A simplified chart of the workflow in this study. The high-resolution image obtained at 2 cm distance provides a “ground truth” of the sample. We then compare the results of linear spectral unmixing of the other two images to the supervised classification using the high-resolution image.

was thus selected as a separate endmember. For the unsupervised classification method, we used the autonomous endmember determination algorithm N-FINDR, a widely applied routine based on the N-volume being largest when taking the purest pixels as spectral endmembers of an N-dimensional dataset (Winter, 1999). We implemented the unsupervised classification with four endmembers, provided that the outcome has reasonable physical interpretations. The four endmembers identified using N-FINDR are named as Dark, Bright, LCP, and HCP, based on their spectral characteristics, respectively. Since the overall reflectance level varied among the three images, possibly due to varying lighting conditions, histogram matching was applied to the medium- and low-resolution image to match the high-resolution image’s reflectance level.

Finally, we performed spectral unmixing for the three images using the selected endmembers. Spectral mixing at visible near-infrared wavelengths could be non-linear due to volumetric scattering, while if the reflectance is dominated by the single scattering of the uppermost layer, a linear-mixing approximation could be reasonable. In order to evaluate the problem to the first order, we performed Fully Constrained Linear Spectral Unmixing (FCLSU) based on a least-squares method (Heinz and Chang, 2001) using both unsupervised and supervised endmembers extracted from the high-resolution image (taken at 2 cm distance). The linear mixing model assumes any reflectance spectrum as a linear combination of the spectra of each pure mineral phases (endmembers) weighted by their abundance.

$$r_{mix}(\lambda) = \sum_{i=1}^N (a_i * r_i(\lambda)) + \eta \quad (1)$$

r_{mix} is the reflectance of the mixture. r_i is the reflectance of each endmember for a total of N endmembers. a_i is the abundance of each endmember. η is the residual noise and modeling error. Additional constraints include the nonnegativity of the abundance and the sum to be 1.

$$a_i \geq 0 \quad \forall i, \quad \sum_{i=1}^N a_i = 1 \quad (2)$$

To validate the results from linear spectral unmixing, we utilized the high-resolution image to make a “spectral endmember classification map” as the ground truth for spectral unmixing. This classification map was made by first selecting the Dark endmember pixels with a minimum threshold of 0.8 in abundance and then assigning all other pixels to the endmember with the highest abundance value in the unmixing results. The minimum threshold is adjusted and then chosen to best match the areal extent of the dark matrix. We thus annotate this

method as the maximum value, dark pixel threshold (MV/DT) method. We use this image as the “ground truth” of the spectral endmember mapping and compare those with the unmixing results from the rest of the data products. We find the mineralogy mapping using the threshold method is appropriate for large pyroxene phenocrysts, as the outlines are clearly visible and the zonation in these phenocrysts are resolved in the image. Although the results differ largely for the bulk percentage, the relative proportion of HCP and LCP remains consistent. However, we note that we cannot resolve the small inclusions of opaque minerals (e.g., Fe-Ti oxides) and they could be partly included in the classification of pyroxene or Dark endmembers. The reported mineralogy in the literature is based on point counts on a polarized or backscatter electron image (e.g., Barrat et al., 2001; Beck et al., 2004) and only reported bulk pyroxene percentages. The prediction from the threshold method is within ~10% comparing to the reported volume percentage of pyroxene.

3. Results

3.1. Datasets and bulk spectra results

False-color composites of data acquired in this study are shown in Fig. 2. On the false-color images, the low calcium pyroxenes appear in pink, high-calcium pyroxenes in green, and the dark matrix in black (Fig. 2).

The porphyritic texture and the pyroxene zonations are visible on the high- and medium-resolution images with spatial resolution of 50 $\mu\text{m}/\text{pixel}$ and 0.2 mm/pixel, respectively. At the spatial resolution of the high-resolution image (~50 $\mu\text{m}/\text{pixel}$), it is possible to discern the pyroxene phenocrysts, while the dark matrix composed of maskelynite, phosphate, and other minerals cannot be resolved. We find the bulk spectra of the image reflect mainly pyroxene spectra, consistent with the meteorite’s bulk composition dominated by pyroxene phenocrysts. Pyroxenes are chain silicates consisting of octahedrons where the metal cations reside, sandwiched between two silicon tetrahedral chains. Typically there are two types of octahedrons in pyroxene, M1 represents the smaller octahedrons whereas M2 is the larger, more irregular octahedron. The 2- μm absorption band shape and position is preferentially determined by the crystal field splitting of Fe^{2+} in the M2 site. The 2- μm band position is located at around 2–2.05 μm for NWA480. The band is relatively wide, which is indicative of a combination of the 2-micron band of LCP and HCP (Sunshine et al., 1999; Mandon et al., 2021). Despite $\leq 5\%$ discrepancies in overall reflectance, the bulk spectra in continuum-removed space overlap with one another, suggesting that

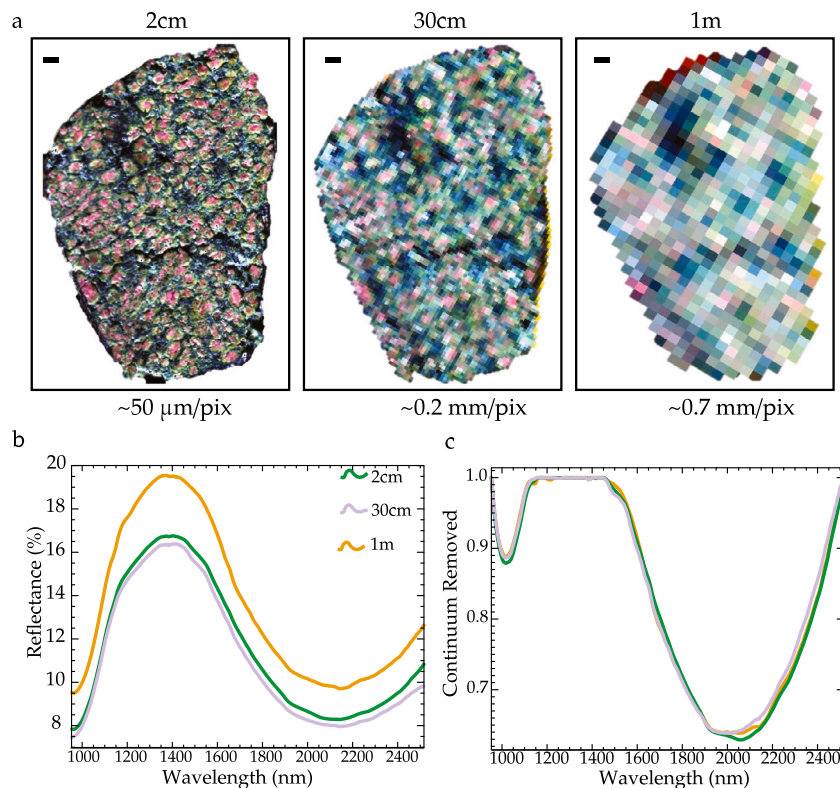


Fig. 2. a. False color combinations of image datasets with different resolutions (Red: 1220 nm, Green: 1656 nm, Blue: 2146 nm). Here the low calcium pyroxenes appear in pink, high-calcium pyroxenes in green, and the dark matrix in black. The black scale bar represents 1 mm. b. Average spectra of the rock surface using three images. c. Normalized reflectance (of spectra in b) using continuum removal. The continuum applied here is a convex hull fit of the spectrum with straightline-segments. The variations at 2.1 μm are caused by the intrinsic spectral feature of the Spectralon target (e.g., Zhang et al., 2014). (For interpretation of the references to color in this figure legend, the reader is referred to the web version of this article.)

the bulk spectra of the meteorite well represent the linear combination of all the pixels regardless of the resolution of the image. Since the number of photons of light reaching the detector should be identical for the same area regardless of standoff distance, the consistency of these measurements is expected. If there are minor differences, it is likely due to the design of detector or slight differences in the measurements, rather than the physics of light interacting with the material differently.

3.2. Spectral endmember extraction and classification map

Spatial heterogeneity at 10 s of micron to millimeter scale contributes to the rock surface's bulk spectra, proportionally to their surface area. If the surface heterogeneity could be reduced into a few spectral endmembers, the bulk spectra should reflect the linear combination of the spectral endmembers. However, identifying and quantitatively modeling spectral mixing in rock slab is difficult to validate since the spectral endmembers are not equivalent to the mineralogy within (Isaacson et al., 2011). The extent to which one could differentiate spectrally distinct components in a rock depends on the reflectance and the absorption features of individual mineral grains and the resolution of the spectral image. Here we discuss the classification results in comparison with volumetric abundances of various minerals since the cross-sectional area is equivalent to the volumetric abundances of various components in a probabilistic sense.

In NWA 480, pyroxenes are identified with three obvious zones: a LCP core (Mg/Ca \sim 20), an augite rim (Mg/Ca \sim 1), and a Fe-pigeonite outer rim (Mg/Ca \sim 0.1) (Barrat et al., 2001). Maskelynite, which composes of 21 vol% of the entire meteorite (Barrat et al., 2001), may have a 1.25–1.3 μm absorption due to minor substitute of Fe in plagioclase. The 1.25–1.3 μm absorption is weakened and broadened under shock-loading and disappears as maskelynite develops (Adams et al., 1979),

while the absorption remains detectable in anorthite-rich rock powders even after shock (Johnson, 2003). Laboratory analysis showed that plagioclase is only diagnostic in mafic mineral mixture containing \leq 10% olivine or pyroxene (Cheek and Pieters, 2014). To differentiate maskelynite from other minerals in the dark matrix would be even harder due to the small signal-to-noise ratio. We used four endmembers in the N-FINDR routine to identify spectral endmembers in the image cube, and based on the endmember spectrum, we identify them as LCP, HCP, Dark and Bright endmembers. We show the spectral endmembers from the unsupervised unmixing results for all three images (Fig. 3). The same endmembers have reduced reflectance with a decreased resolution, and the minor component (e.g., Bright endmember) cannot be distinguished in the low-resolution image. As a result, the unmixing of the low-resolution image picks up the sample holder's absorption features in mixture with pyroxene as an additional endmember. Subsequently, only endmembers selected in the high-resolution image are used for unmixing analysis.

We selected five spectrally distinctive endmembers in the supervised method, including LCP, HCP, Dark HCP, Dark, and Bright endmembers. Among these five endmembers, the Dark HCP endmember mapped the outer rims of pyroxene phenocrysts with a Fe-pigeonite composition and was not included in the unsupervised classification. The Dark HCP endmember cannot be differentiated from the Dark endmember in the unsupervised endmember extraction by adding more spectral endmembers because of the low reflectance and lack of contrast between the Dark HCP and Dark endmembers. The classification based on the high-resolution image is shown in Fig. 4 for unsupervised and supervised classification. As expected, the supervised version provides a more accurate classification of the pyroxenes' zonation since three different pyroxene spectral endmembers were used. However, when it comes to

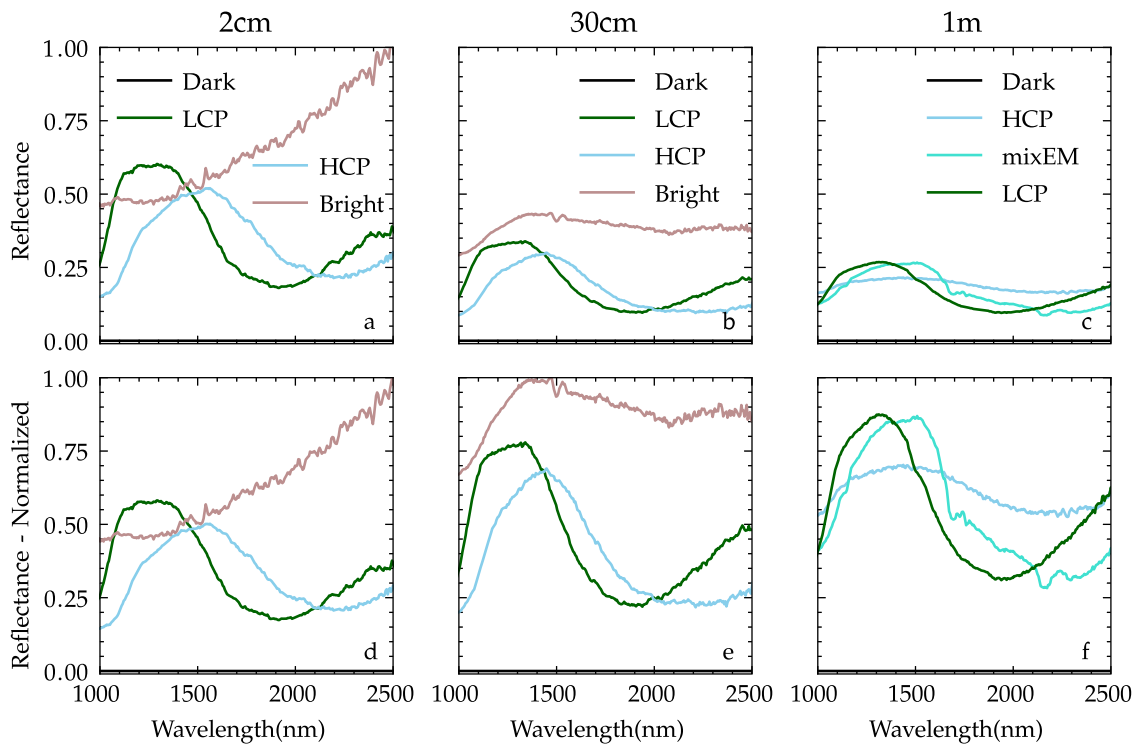


Fig. 3. Spectral endmember extraction for images of different resolution (with distance at 2 cm, 30 cm, 1 m) on original (upper panel: sub-figures a, b, c) and normalized (lower panel: figures d, e, f) datasets, respectively. In the low-resolution image, a few pixels on the margin still preserve minor absorption features caused by subpixel mixing of the sample holder, highlighted in the mixed endmember (mixEM).

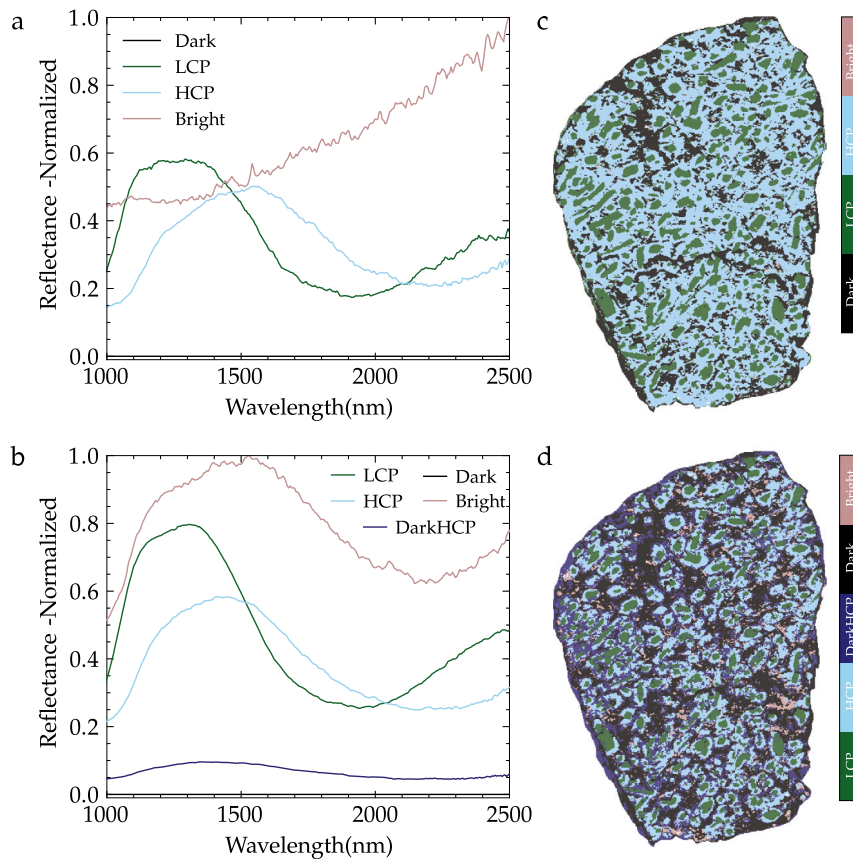


Fig. 4. Spectral endmember extraction and spectral classification map with dark endmember threshold and maximum value (See Section 2.2 for details). a. Normalized spectral endmembers from the automated extraction using N-FINDER routine. b. Normalized spectral endmembers selected manually for supervised classification. c. Classification map of the high-resolution image with endmembers selected with N-FINDER (a). d. Classification map of the high-resolution image with supervised endmember selection (c).

Table 1

Result of spectral unmixing using the unsupervised method. The numbers represent the percentage of an endmember in the entire image. (Acronyms: MV = maximum value, DT = Dark pixel threshold, FCLSU = fully constrained linear spectral unmixing). Bulk spectrum for unmixing is from the high-resolution image (See Fig. 2). As a comparison, previous petrography study with point counting method reported pyroxenes count to 72% volume percentage in this sample.

IMAGE	High-res	High-res	Med-res	Low-res	Bulk
RESOLUTION	50 μm	50 μm	0.2 mm	0.7 mm	~2 cm
Method	MV/DT	FCLSU	FCLSU	FCLSU	FCLSU
LCP	21.68	13.05	9.12	8.75	10.66
HCP	54.31	18.33	13.15	12.16	15.44
Dark	23.56	66.60	76.65	78.35	73.10
Bright	0.45	2.02	1.08	0.74	0.80
Total pyroxene	75.99	31.38	22.27	20.91	26.10

Table 2

Result of spectral unmixing using the supervised method. The numbers represent the percentage of an endmember in the entire image. (Acronyms: MV = maximum value, DT = Dark pixel threshold, FCLSU = fully constrained linear spectral unmixing). Bulk spectrum for unmixing is from the high-resolution image (See Fig. 2). As a comparison, previous petrography study with point counting method reported pyroxenes count to 72% volume percentage in this sample.

IMAGE	High-res	High-res	Med-res	Low-res	Bulk
RESOLUTION	50 μm	50 μm	0.2 mm	0.7 mm	~2 cm
Method	MV/DT	FCLSU	FCLSU	FCLSU	FCLSU
LCP	12.36	5.72	4.64	4.58	3.65
HCP	26.60	10.75	9.25	9.65	3.12
Dark HCP	22.57	12.67	4.66	3.36	68.38
Dark	33.62	65.64	78.81	80.67	22.56
Bright	4.85	5.21	2.64	1.74	2.28
Total pyroxene	61.53	29.14	18.55	17.59	75.17

the total amount of pyroxene (sum of LCP, HCP, and Dark HCP), the supervised classification sums up to ~62% of the entire rock surface (Table 2). In contrast, the unsupervised classification result (~76%) (Table 1) is a better estimate, close to the petrologic classification. The sum of total pyroxene is a measure of how well the classification does for the Dark and Bright endmembers, with more subtle spectral features. Due to the close resemblance between the Dark HCP and Dark endmember and the bright LCP pixels and the Bright endmember, misclassifications at ~10% level cannot be improved using the spectral dataset alone.

3.3. Spectral unmixing results

In the case of planetary applications, the spatial, heterogeneous mixture is inevitable. Assuming the different spectral components in the dataset combine linearly, it is theoretically possible to decompose the coarser-resolution images and invert each spectral component's percentages. We performed spectral unmixing of the three image datasets using the same endmembers, manually selected on the high-resolution image, to evaluate if it is possible to scale up the expected results from linear spectral mixing (Tables 1, 2). Interestingly, the resulting classifications in the supervised case are consistent within 2% for LCP and HCP among the three images using the FCLSU method, and the relative proportion of HCP and LCP is consistent in both methods (Fig. 5).

However, Dark and Dark HCP endmembers' abundances are inconsistent between the high-resolution image and the other two images. A possible explanation is that the Dark and Dark HCP endmembers may only be differentiated if they occur as pure pixels in high-resolution data but cannot be differentiated in lower-resolution datasets when they are considered as a linear mixture. None of the FCLSU results match well that of the supervised classification using maximum values and dark pixel threshold methods (Fig. 4d), and the most considerable discrepancy among the results lies in the classification of the Dark endmember. The same trend is found for the unsupervised classification,

where LCP and HCP results are consistent among different resolution images, and the MV/DT (Maximum value, Dark pixel threshold) image accounts for fewer Dark pixels, so the total pyroxene is higher. We note here in both types of classification results, spectral unmixing of medium- and low-resolution images underestimate LCP and HCP compared to the high-resolution image using the same classification method (Tables 1, 2).

In order to test the effect of the Dark endmember, we performed spectral unmixing without the Dark endmember (with HCP, LCP, Dark HCP and Bright). In this case, the resulting abundances would regroup ~25% of maskelynite and opaque minerals into pyroxenes (mostly Dark HCP), ending up with close to 100% pyroxene. Therefore, the presence or absence of a Dark endmember would either underestimate or overestimate the abundances for pyroxenes, due to the predominance of dark component in the rock. There is currently no good solution to overcome the internal variability in the mineral grains.

4. Discussion

4.1. Effects of spectral mixing in rock slabs

Here we discuss the underlying assumptions and reasoning to decompose the bulk rock spectra through linear deconvolution. As we observe, significant microscopic spatial heterogeneities occur in igneous rocks (and some sedimentary rocks). Such spatial heterogeneity is typical of planetary surfaces. The underlying assumption is such that at detector resolution, each pixel that can resolve the mineral size has a spectrum that are close to those of the same type of mineral grains. This assumption would be true if the spectral data are dominated by single-scattered light (light only interacted with the first mineral grain).

For visible-near-infrared wavelengths and the typical extinction coefficient (α) in minerals measured in the laboratory, volumetric scattering is expected (Hapke and Wells, 1981; Hapke, 1981; Clark et al., 1990). For example, pyroxenes have an imaginary optical constant (k) of $10^{-4} - 10^{-5}$ at wavelengths (λ) of 1–2 μm (Lucey, 1998). For a grain size of 1 mm, the internal transmission factor can be approximated as: $\alpha\langle D \rangle = \frac{4\pi k D}{\lambda} = 0.12 - 1.25$. Here $\langle D \rangle$ is the average distance traveled by transmitted rays during one traverse of the particle, approximate as the grain size (D). The corresponding transmission factor of such a pyroxene crystal using the exponential model is: $\theta = e^{-\alpha\langle D \rangle} = 0.29 - 0.88$. A significant portion (29%–88%) of the light should be transmitted through the pyroxene, interacting with the neighboring minerals.

However, naturally occurring minerals with possible internal scatterers like mineral/liquid/gas inclusions as well as fractures and defects inside mineral structure may greatly increase the extinction coefficient of the mineral grains, especially when the phenocrysts are relatively large ($D = 0.5 - 1$ mm) (Roedder, 1965; Anderson and Wright, 1972; Tait, 1992; Danyushevsky et al., 2002). Such inclusions in phenocrysts of igneous rocks are often transitional metal-bearing oxides (e.g., magnetite (Fe_3O_4), ilmenite (FeTiO_3), chromite (FeCr_2O_4)) (Fleet et al., 1980; Scowen et al., 1991) with important absorption features due to electronic transition and charge transfer in the visible-near-infrared wavelength range, resulting in overall reduced single scattering albedo of the mineral. The effects of intimate mixing could be dominating in the fine-grained portion of the matrix groundmass, where a small amount of opaque minerals significantly reduces the contrast, resulting in an overall low albedo of the mixture. As a combined effect, the spectral reflectance and absorption features of the linear combination of the phenocryst and the matrix are dominated by the pyroxene component. Light scattered via single or multiple scattering inside large phenocrysts is likely the dominating factor for spectral response in porphyritic igneous rocks, lending support to the linear deconvolution of martian meteorite hyperspectral image.

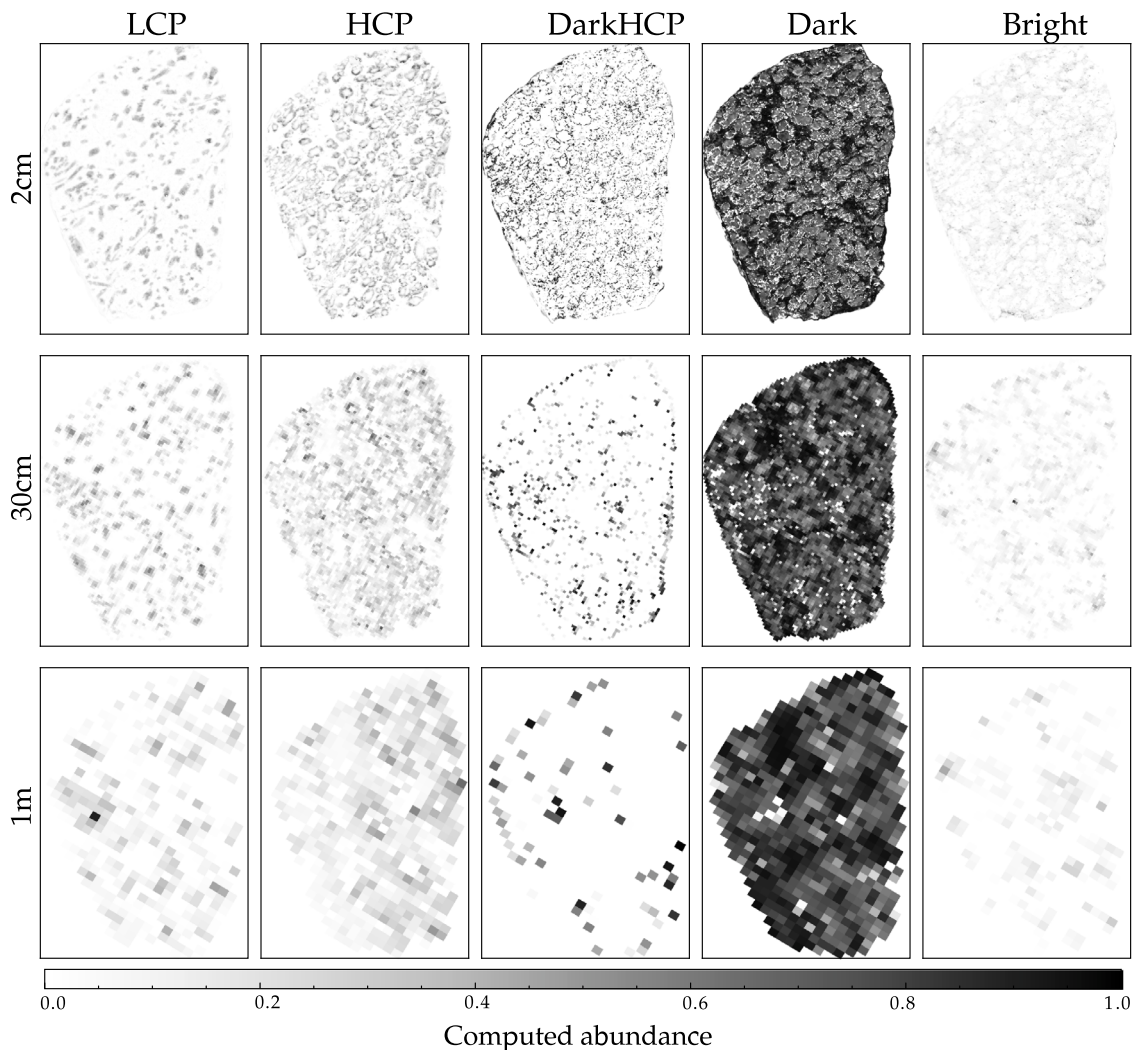


Fig. 5. The linear unmixing results using FCLSU for the five spectral endmembers selected using the supervised method.

Similar to previous work (Pompilio et al., 2007; Carli et al., 2014; Mandon et al., 2021) on spectra for rock slabs, we find the large phenocrysts dominate bulk spectra of the rock slab, contrary to a granular mixture where smaller grain size components dominate the spectral response due to an increased number of multiple scattering events. However, assuming the same total volume of phenocrysts, varying the size of the phenocrysts alone cannot explain the different behavior. Here we propose that the dominating effect of phenocrysts results from the greater number of internal scatterers, causing the diverging behavior of scattering. Since large phenocrysts are mostly polycrystalline, grain boundaries, small inclusions and fractures/cracks would be more common than smaller grains. These scatterers result in increased internal scattering within larger phenocrysts and therefore less efficient transmission of light. Further investigation into natural samples is needed to enlighten the controls on the varying scattering behavior.

4.2. Uncertainties in linear unmixing and spectral variability

It is possible to reduce the spectral unmixing problems into simple linear unmixing assuming single scattering is the dominant factor. The abundances of each spectral endmember can then be calculated using the spectra of the mixture. We show in the results that linear unmixing of NWA 480 vastly underestimates the abundances of

pyroxene phenocrysts, which is likely due to the misclassification of dark pyroxene pixels as “Dark” endmember since the variations in spectral reflectance are mistakenly interpreted as a linear combination of the Dark endmember and the other brighter endmembers (Tables 1, 2). Notably, the large pyroxene phenocryst’s outer rim is a Fe-rich pigeonite with low reflectance ($\leq 15\%$) that cannot be readily distinguished from the “Dark” endmember commonly found in the matrix. The statistics of each spectral class in Fig. 6 highlight the significant overlap between different classes. Such large endmember variabilities that transcend different groups of minerals prevent an accurate unmixing, especially when the spectral endmembers (e.g., Dark) are relatively featureless (lack of spectral absorption features). Even the LCP endmember, with the most robust absorption features and the most confident classification results, shows variations in reflectance up to 45%.

Spectral unmixing algorithm studies for hyperspectral images have identified spectral variability as a major issue in retrieving abundances (Koirala et al., 2020; Drumetz et al., 2016, 2019; Borsoi et al., 2020a). The variability comes from external factors (atmospheric and illumination conditions, topographic variations) and intrinsic variability inside the samples, where the controlling physicochemical parameters are usually unknown (Borsoi et al., 2020b). Recently developed algorithms account for endmember variability using endmember bundles, computational or parametric models (e.g., Drumetz et al., 2016,

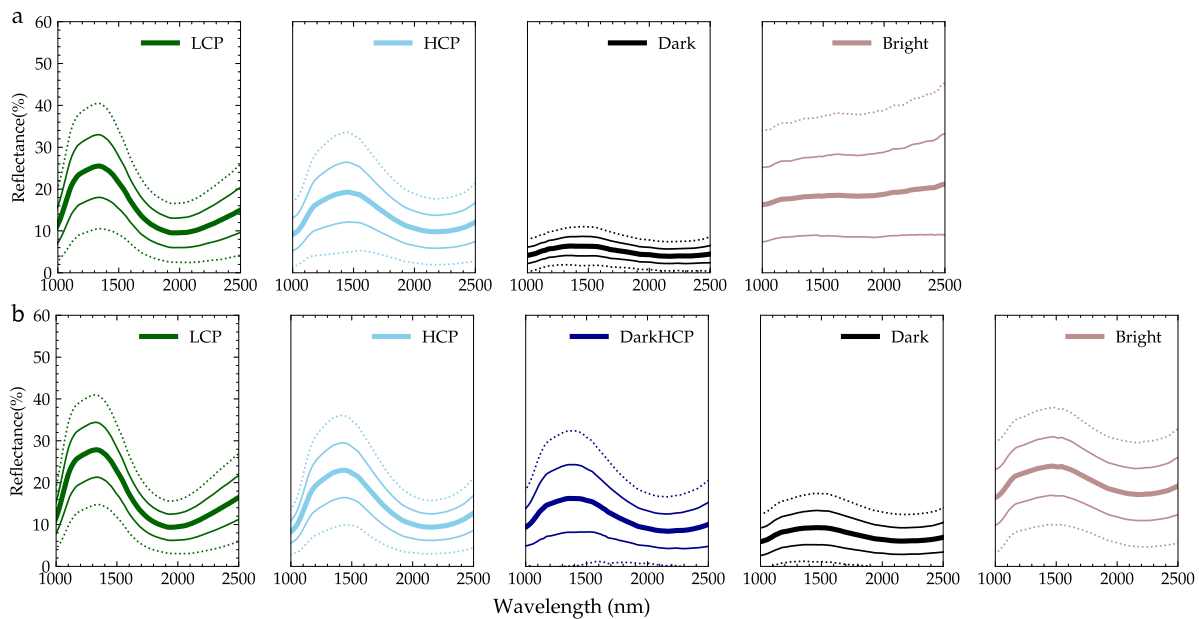


Fig. 6. Class statistics of a. unsupervised classification and b. supervised classification. Spectral statistics were calculated using all the pixels labeled in each class using the dark-pixel threshold and maximum value method (Fig. 4). Thick solid lines represent the mean value of each endmember (μ); Thin solid lines represent mean value ± 1 standard deviation ($\mu \pm \sigma$); Dashed lines represent ± 2 standard deviations ($\mu \pm 2\sigma$).

2019; Borsoi et al., 2020b, and references therein). Understanding the causes for such variability in the laboratory/field can be crucial for developing precise algorithms and analysis (Drumetz et al., 2019), as such models for spectral variability have been developed for vegetation and canopy studies (Asner, 1998). We discuss below the possible causes for spectral variability in natural samples that are directly relevant to geologic investigations.

4.3. Possible causes for spectral variability in minerals

There are three types of causes for spectral variability that may occur for the same mineralogy: variations in chemical composition, geometrical configurations, and the internal scatterers of the mineral grains. Compositional variations often occur in igneous minerals due to the reaction with the surrounding melt with time-dependent composition changes during fractional crystallization. For igneous rocks that have experienced aqueous alteration, dissolution and diffusion of chemical species can also form alteration rims around mineral grains or along fractures, with different optical properties in the unaltered/pristine interior. Such composition-caused spectral variability is often evident in the absorption band centers' position and overall reflectance for large phenocrysts. For example, in the pyroxene phenocrysts of NWA 480, the band center shifts from ~ 1.9 to $2.1 \mu\text{m}$ from the core to the rim (Fig. 7).

The shift in band center corresponds well to the previous chemical analysis of the meteorite (Barrat et al., 2001, 2002) where the pyroxene phenocrysts have a low-calcium core, an augite rim, and a Fe-pigeonite outer rim. Chemical zoning also results in variability in overall reflectance. For example, with a $2 \mu\text{m}$ band position similar to the inner core, the Fe-rich outer rim has a much lower reflectance, likely due to the increased content of Fe and possible Fe-oxide inclusions.

Other than the chemical variations within the mineral crystals, the interaction of light with the cut surface can be influenced by the crystal's geometry and physical properties. Specifically, possible influencing factors include (a) the lighting and observing geometry, (b) the surface roughness, (c) the phenocryst orientation, (d) the grain size of the phenocryst. In our experiment, each pixel is obtained with the same lighting geometry. There is no documented surface roughness

of the slab surface, but surface roughness at a micron-meter scale cannot be directly constrained. To better understand the effect of the phenocryst grain size, we extracted average spectra on each LCP core and examined regional variations in reflectance levels, but no regional variation is noted (Fig. 8).

To further evaluate the variability due to grainsize, we derived the size of the LCP core and its average spectra in the 2 cm dataset. We extracted the LCP core pixels from the supervised classification result (Fig. 4d). The grainsize d is then computed as $d = 2 * \sqrt{A/\pi}$, where A is the areal extent of the core pixels, simulating the diameter of a circle that matches the measured area. The average spectra of each grain are used to perform the spectral analysis in Fig. 9. We find that the reflectance value does not change according to grain size but instead remains constant or slightly decreasing toward smaller LCP grains (Fig. 9). Contrary to the intimate mixing model (See Appendix for detail), the lack of variation in the reflectance level for most pyroxenes indicates that single scattering or scattering within the phenocryst is the dominant component in reflectance (Fig. 9). There is a slight reflectance decrease with decreasing grain size. Such a trend could be better explained by considering the transparent pyroxene as an equivalent slab that overlies the dark matrix, so a smaller grain size indicates a shorter path length and reduced absorption (Hapke, 2012). In addition, roughness, crystal orientation, or fractures and inclusions (Beck et al., 2004) may also contribute to the variability with grainsize.

Finally, the internal scatterers, including fractures and inclusions, would increase scattering and absorption within the phenocrysts depending on their compositions and significantly modify the resulting spectra depending on the types of inclusions. For example, gas and fluid inclusions can be approximated as isotropic scatterers and non-absorbing in the visible wavelength range, increasing the internal scattering and enhancing the spectral feature of large phenocrysts. In the infrared, inclusions can be highly absorbing in specific wavelengths depending on the liquid/gas species. In the meantime, mineral inclusions like Fe-Ti oxides, chromite and pyrrhotite are often opaque (e.g., Adams, 1974) due to the electronic transition and charge transfer occurring in the visible wavelength, as shown in the Backscattered electron (BSE) image (Fig. 10), taken with a JEOL JSM6301-F scanning electron microscope (SCIAM, Angers) (Barrat et al., 2002; Beck et al.,

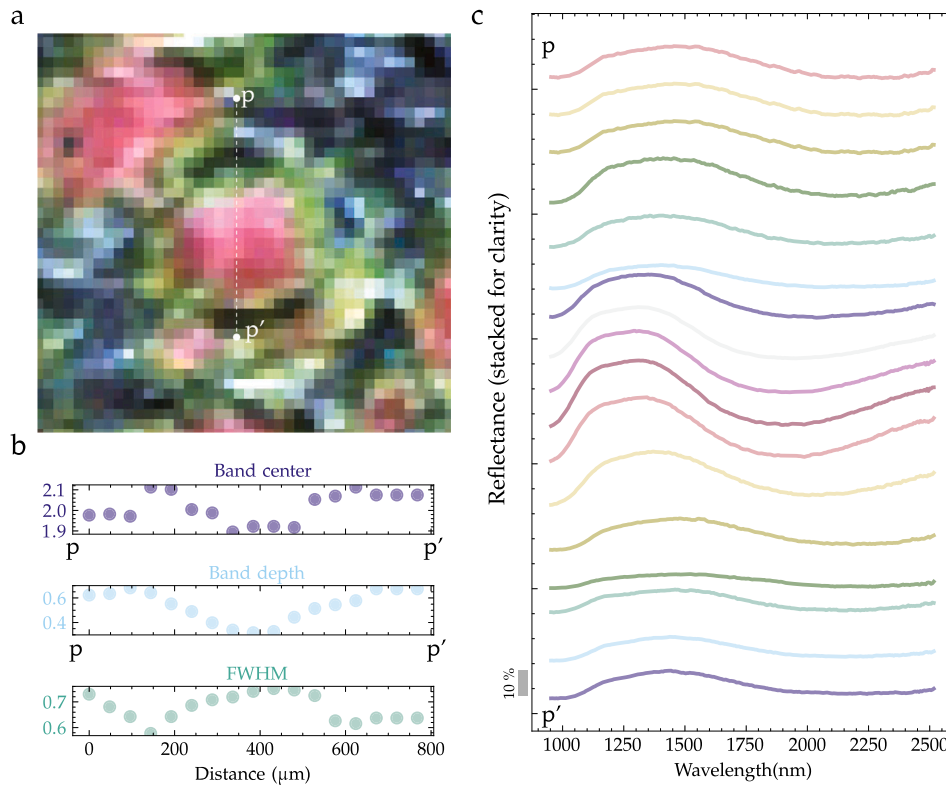


Fig. 7. Rim-to-rim profile of the pyroxene phenocryst in NWA 480. a. False color image of a pyroxene phenocryst (Red: 1220 nm, Green: 1656 nm, Blue: 2146 nm). b. The band center, the band depth, and full width half minimum of the 2 μm band along the p-p' profile highlighted in a. c. Spectral data extracted in the high-resolution image along the p-p' profile shown in a, showing the variability due to chemistry. (For interpretation of the references to color in this figure legend, the reader is referred to the web version of this article.)

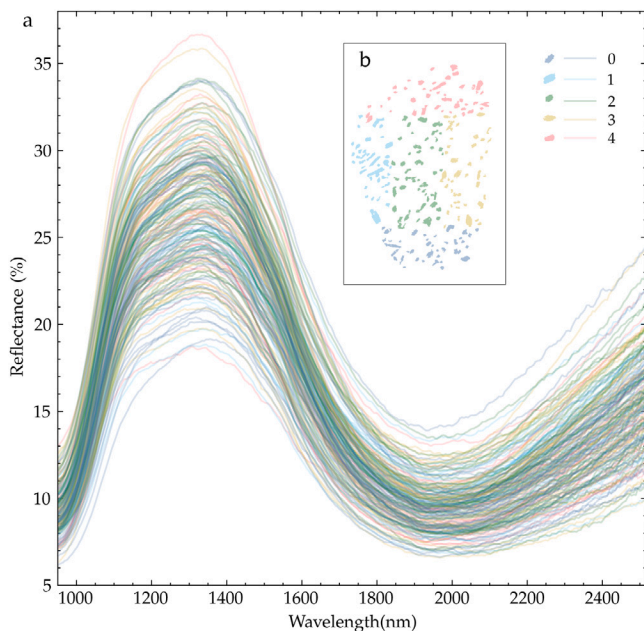


Fig. 8. a. Average spectral plot of LCP core pixels. Different colors signify five spatially divided regions of the rock surface: Numbered 0–4. b. The map of LCP grains of the five divided regions. Note there is no preferential bias on the location in terms of spectral variability.

2004). Detailed, quantitative chemical analysis at the micron-meter scale is needed to show the related inclusions which may have caused such variability.

Despite the intrinsic complexity of inclusions in the minerals, physical and petrological models that account for internal scatterers in minerals in different geological contexts would be very useful for spectral analysis and unmixing, as similar models were made for varying amounts of aerosols in the atmosphere (Mishchenko et al., 1999); or impurities in ice slabs (Andrieu et al., 2015).

4.4. Difficulties and implications for quantitative analysis of planetary surfaces

Planetary surfaces are commonly composed of rocky material rather than particulates of separate, pure mineral grains. Therefore, understanding spectral mixing in rock slabs is the first step toward a more quantitative analysis of the spectral reflectance dataset. Microscopic analysis of rocks shows various textures and structures representing spatial heterogeneity, which is not currently considered in a homogeneous mixing model. Additionally, we have shown that even for the same type of mineral grains, the reflectance level varies up to 45%, and the existence of opaque or transparent minerals without any spectral absorption features contribute to ambiguity in classification.

Given these observations, we discuss the fundamental uncertainties that are crucial to address through quantitative spectral unmixing igneous rocks.

First, the existence of opaque and dark minerals, including but not limited to Fe-Ti oxides, chromite, sulfide, glass (maskelynite), needs to be considered, in particular when considering igneous rocks (Pompilio et al., 2007; Carli et al., 2014, 2015; Serventi et al., 2013). The abundance of opaque minerals would be challenging to retrieve since

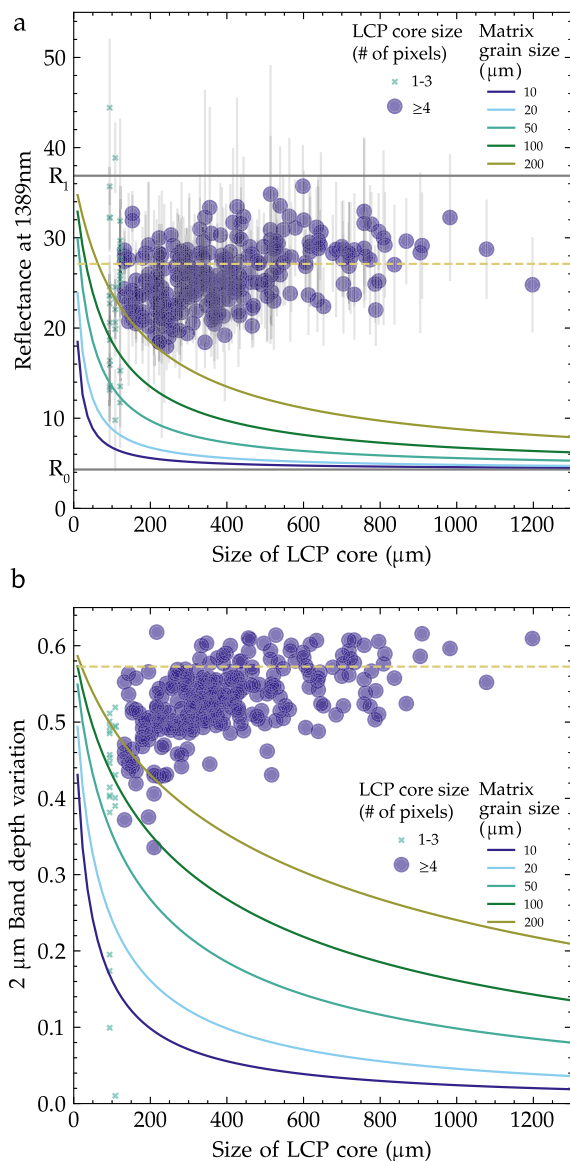


Fig. 9. a. Reflectance variations in pyroxene phenocrysts at 1389 nm. Purple dots represent the average reflectance of phenocrysts plotted against its grain size. The error bars represent the 1- σ reflectance variation within the same phenocryst. b. Band depth of the 2 μm band calculated using a standard band depth function ($BD = 1 - R/R_c$) with fixed endpoints at 1.225 and 2.516 μm evaluated at 1.933 μm . LCP cores that cover less than three pixels are shown in green crosses, highlighted due to possible misclassifications for smaller grains. The gray solid lines in a. represents the reflectance of the phenocryst (R_0) and the matrix (R_1), calculated for two spectral endmembers of single scattering albedo of 0.9 and 0.3, respectively. The yellow dashed line represents the average of a linear mixture 70% phenocryst and 30% matrix. Colored solid lines correspond to non-linear mixing results based on Hapke's model, given various matrix grain sizes.

there is often a lack of spectral feature or that the spectral absorptions are unintelligible due to the small signal-to-noise ratio. These minerals contribute to the bulk rock spectra typically by changing the rock's total reflectance, an effect indistinguishable from variations in physical parameters (e.g., surface roughness, illumination, and observation conditions). Non-linear spectral unmixing calculations using only one or a few selected dark mineral (e.g., basaltic glass) may tend to add weight to the weak spectral features even though they are unlikely to be the dominating feature in a spatially heterogeneous mixture due to their small contribution to the bulk rock abundance and reflectance.

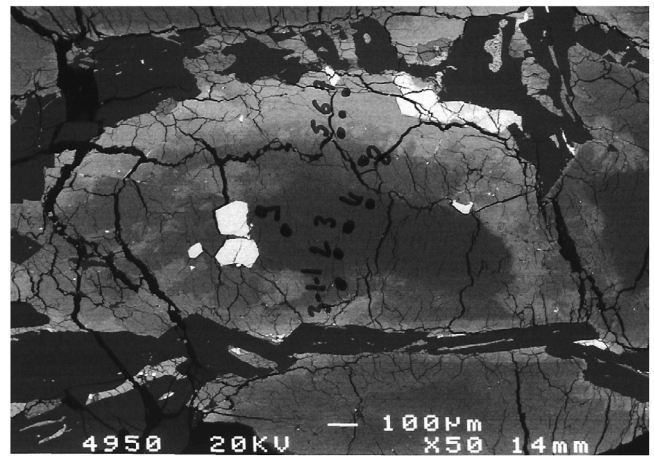


Fig. 10. SEM image of one pyroxene phenocryst in the meteorite NWA 480 (Barrat et al., 2001; Beck et al., 2004). Here the large crystal in the center is the pyroxene phenocryst with zonation. Bright zones indicate minerals with high electron density, often Fe-Ti oxides, pyrrhotite, and chromite. The few bright isometric minerals inside pyroxene are likely chromite, which formed around the same time as the pyroxene LCP core (Barrat et al., 2001). Various dark fractures are visible at this scale inside the pyroxene phenocryst.

Second, the spectral variability in different grains of the same mineral induces errors regardless of linear or non-linear spectral unmixing models and needs to be better understood. These grains can be differentially altered chemically and physically due to varying grain size, causing spectral variability. The spectral variability induced by zoning, fracturing, and internal scatterers need to be quantified with specifically designed experiments and measurements. For example, previous studies on the solid solution in olivines (Isaacson et al., 2014), clinopyroxenes (Klima et al., 2011) and orthopyroxenes (Wang et al., 2005; Dyar et al., 2007) have shown the effect of temperature and melt composition on the site occupation of Fe^{2+} and Mg. If the lithology under investigation is different from a basaltic igneous rock, the mineralogy and causes for spectral variability may need to be reconsidered. For example, if an altered rock sample has only a small fraction (<10%) of dark component, this endmember may be ignored, and the linear unmixing may provide reasonable estimates for the image based on the sharp vibrational absorption bands due to metal-OH and H_2O combination tones (e.g., Leask and Ehlmann, 2016).

Despite the foreseeable challenges in data interpretation, infrared spectrometers are one of the most important tools to determine mineralogy for *in situ* exploration, and have been included in the instrument payload onboard Martian rovers, for example, SuperCam instrument onboard Mars 2020 Perseverance rover (Wiens et al., 2020; Maurice et al., 2021), the MarSCoDe instrument onboard Tianwen-1 Zhurong rover (Wan et al., 2021) and Ma_Miss instrument onboard ExoMars 2022 Rosalind Franklin rover (De Sanctis et al., 2017). In addition to point spectrometers, a microimaging spectrometer will also be carried onboard ExoMars 2022 (MicrOmega) (Bibring et al., 2017). Spectral mixing at microscopic scale would inevitably impact the resulting measurement. Based on our analysis, we speculate that for igneous rocks on Mars, the phenocrysts situated in a dark matrix would often dominate the contribution to the bulk spectra. We would recommend when taking spectral measurements *in situ*, texture and albedo contrast between phenocryst and matrix should be determined using high resolution images (e.g., by the SuperCam Remote Micro-imager (RMI) or MicrOmega). Then spectral unmixing can be made for an accurate interpretation of the rock petrology and composition with a pre-defined percentage of the dark matrix. We would also emphasize that nonlinear mixing models are better suited to the deconvolution of particulate

mixture spectra (e.g., regolith), and caution should be taken before application to the spectra of bulk rocks.

Although spectral measurements of natural samples would always suffer from the spatial heterogeneity and spectral variability, texture and physical/chemical variations in igneous rocks should not be considered as random parameters. Predictions based on igneous minerals' evolution along various pressure and temperature pathways would help build a petrologically reasonable model for spectral endmember variability. Hyperspectral imaging in the laboratory also provides a novel approach to test spectral mixing in natural samples with spatial context. Spectral imaging data of natural samples with known geological background would provide more quantitative constraints on the causes and extent of spectral variability. Combining with statistical analysis, such study would pave the way for an improved quantification of planetary surface materials in the future.

5. Conclusion

In summary, based on newly acquired hyperspectral measurements at different scales, we performed classification and unmixing analysis of the hyperspectral image cubes to understand better the parameters that affect spectral mixing in a rock slab. We find that a linear combination of each pixel gives a reasonable prediction for the rock's bulk spectrum. However, different endmembers' spectral variability prevents an accurate quantitative assessment, vastly underestimating the phenocrysts' contribution when a Dark endmember is included. In this dataset, the spectral variability in the pyroxene phenocrysts may be due to the chemical zonation, mineral lattice orientation, and the presence of inclusions and fractures. The varying grain size or geometric parameters are not the main factors that result in spectral variability in the pyroxene phenocrysts. Our work shows a new approach using hyperspectral images at the microscale to understand radiative transfer models at different scales. As current and future planetary missions will be carrying visible-near-infrared spectrometers to investigate the composition of rocks *in situ*, this analysis opens a new approach to understanding rock composition and texture from infrared spectra. Further investigations will be focused on better understanding the physical and chemical variability within the framework of the rock's petrological history.

Acknowledgments

The datafiles used and processed in this work will be available online at <http://doi.org/10.5281/zenodo.4459182>. We thank the ANR project ANR-18-ERC1-0005 and Carlsberg Foundation, Denmark grant CF18_1105 for supporting this work. We thank in particular Lukasz Paluchowski from HySpex for his help in making the measurements. We also appreciate J.-A. Barrat, M. Tetley, and T. Bodin's inputs about samples and data analysis methods.

Appendix. Intimate mixture modeling

We applied the Hapke theory (Hapke, 1981; Hapke and Wells, 1981; Hapke, 1984) for intimate mixing of particulate minerals to highlight the effect of mixing for various grain sizes (Fig. 9). We assumed a constant single scattering albedo for the mean grain size. The grain size did not change the apparent single scattering albedo but only resulted in the varying geometric cross-section with which light interacts. This choice was made to show increased scattering with smaller grain sizes predicted by intimate mixing. Adding the grain size dependence of single scattering albedo only strengthens the increased scattering trend for smaller grains. Based on Hapke's theory for intimate mixture (Hapke, 2012), the bidirectional reflectance of the mixture is approximated by

$$r_{mix}(i, e, g) = \frac{\omega_{mix}}{4\pi} \frac{\mu_0}{\mu_0 + \mu} [P(g) + H(\mu)H(\mu_0) - 1]. \quad (3)$$

Here ω_{mix} is the single scattering albedo of the mixture, μ_0 and μ are the cosines of the incidence and emergence angle. $P(g)$ is the phase function, H is the Chandrasekhar function.

$$\omega_{mix} = \frac{\omega_1 + C\omega_2}{1 + C} \quad (4)$$

C is the weighting factor:

$$C = \frac{M_1 \rho_2 D_2}{M_2 \rho_1 D_1} \quad (5)$$

Here M is the mass fraction, ρ is the solid density, and D is the grainsize of the component.

References

- Adams, J.B., 1974. Visible and near-infrared diffuse reflectance spectra of pyroxenes as applied to remote sensing of solid objects in the solar system. *J. Geophys. Res.* (1896–1977) (ISSN: 2156-2202) 79 (32), 4829–4836. <http://dx.doi.org/10.1029/JB079i032p04829>.
- Adams, J.B., Hörz, F., Gibbons, R.V., 1979. Effects of shock-loading on the reflectance spectra of plagioclase, pyroxene and glass. In: *Proceedings for Lunar and Planetary Science Conference. Lunar and Planetary Institute, Texas.*
- Anderson, A.T., Wright, T.L., 1972. Phenocrysts and glass inclusions and their bearing on oxidation and mixing of basaltic Magmas, Kilauea Volcano, Hawaii. *Am. Mineral.* (ISSN: 0003-004X) 57 (1–2), 188–216.
- Andrieu, F., Douté, S., Schmidt, F., Schmitt, B., 2015. Radiative transfer model for contaminated rough slabs. *Appl. Opt.* (ISSN: 2155-3165) 54 (31), 9228–9241. <http://dx.doi.org/10.1364/AO.54.009228>.
- Asner, G.P., 1998. Biophysical and biochemical sources of variability in canopy reflectance. *Remote Sens. Environ.* 64 (3), 234–253.
- Barrat, J.A., Gillet, P.H., Sautter, V., Jambon, A., Javoy, M., Göpel, C., Lesourd, M., Keller, F., Petit, E., 2001. The basaltic shergottite North West Africa 480: Petrology and geochemistry. *Meteorit. Planet. Sci. Suppl.* 36, A14.
- Barrat, J.A., Gillet, P., Sautter, V., Jambon, A., Javoy, M., Göpel, C., Lesourd, M., Keller, F., Petit, E., 2002. Petrology and chemistry of the basaltic shergottite North West Africa 480. *Meteorit. Planet. Sci.* 37 (4), 487–499.
- Beck, P., Barrat, J.A., Chaussidon, M., Gillet, P., Bohn, M., 2004. Li isotopic variations in single pyroxenes from the Northwest Africa 480 shergottite (NWA 480): A record of degassing of Martian magmas? *Geochim. Cosmochim. Acta* 68 (13), 2925–2933.
- Bibring, J.-P., Hamm, V., Pilorget, C., Vago, J.L., the MicrOmega Team, 2017. The MicrOmega investigation onboard ExoMars. *Astrobiology* (ISSN: 1531-1074) 17 (6–7), 621–626. <http://dx.doi.org/10.1089/ast.2016.1642>.
- Bibring, J.-P., Langevin, Y., Mustard, J.F., Gendrin, A., Gondet, B., Mangold, N., Pinet, P., Forget, F., 2006. Global mineralogical and aqueous mars history derived from OMEGA/Mars Express Data. *Science* 312, 6.
- Borsoi, R.A., Imbiriba, T., Bermudez, J.C.M., 2020a. A data dependent multiscale model for hyperspectral unmixing with spectral variability. *IEEE Trans. Image Process.* 29, 3638–3651.
- Borsoi, R.A., Imbiriba, T., Bermudez, J.C.M., Richard, C., Chanussot, J., Drumetz, L., Tourneret, J.-Y., Zare, A., Jutten, C., 2020b. Spectral variability in hyperspectral data unmixing: A comprehensive review. *arXiv preprint arXiv:2001.07307*.
- Carli, C., Ciarniello, M., Capaccioni, F., Serventi, G., Sgavetti, M., 2014. Spectral variability of plagioclase–mafic mixtures (2): Investigation of the optical constant and retrieved mineral abundance dependence on particle size distribution. *Icarus* 235, 207–219.
- Carli, C., Serventi, G., Sgavetti, M., 2015. VNIR spectral characteristics of terrestrial igneous effusive rocks: Mineralogical composition and the influence of texture. *Geol. Soc. London Spec. Publ.* (ISSN: 0305-8719) 401 (1), 139–158. <http://dx.doi.org/10.1144/SP401.19>, 2041–4927.
- Cheek, L.C., Pieters, C.M., 2014. Reflectance spectroscopy of plagioclase-dominated mineral mixtures: Implications for characterizing lunar anorthosites remotely. *Am. Mineral.* 99 (10), 1871–1892.
- Clark, R.N., King, T.V.V., Klejwa, M., Swayze, G.A., Vergo, N., 1990. High spectral resolution reflectance spectroscopy of minerals. *J. Geophys. Res.: Solid Earth* (ISSN: 2156-2202) 95 (B8), 12653–12680. <http://dx.doi.org/10.1029/JB095iB08p12653>.
- Cord, A.M., Pinet, P.C., Daydou, Y., Chevrel, S.D., 2003. Planetary regolith surface analogs: Optimized determination of Hapke parameters using multi-angular spectro-imaging laboratory data. *Icarus* (ISSN: 0019-1035) 165 (2), 414–427. [http://dx.doi.org/10.1016/S0019-1035\(03\)00204-5](http://dx.doi.org/10.1016/S0019-1035(03)00204-5).
- Crowley, J.K., 1986. Visible and near-infrared spectra of carbonate rocks: Reflectance variations related to petrographic texture and impurities. *J. Geophys. Res.: Solid Earth* (ISSN: 2156-2202) 91 (B5), 5001–5012. <http://dx.doi.org/10.1029/JB091iB05p05001>.

- Danyushevsky, L.V., McNeill, A.W., Sobolev, A.V., 2002. Experimental and petrological studies of melt inclusions in phenocrysts from mantle-derived magmas: An overview of techniques, advantages and complications. *Chem. Geol.* (ISSN: 0009-2541) 183 (1), 5–24. [http://dx.doi.org/10.1016/S0009-2541\(01\)00369-2](http://dx.doi.org/10.1016/S0009-2541(01)00369-2).
- De Sanctis, M.C., Altieri, F., Ammannito, E., Biondi, D., De Angelis, S., Meini, M., Mondello, G., Novi, S., Paolinetti, R., Soldani, M., Mugnuolo, R., Pirrotta, S., Vago, J.L., the Ma_MISS team, 2017. Ma_MISS on ExoMars: Mineralogical characterization of the martian subsurface. *Astrobiology* (ISSN: 1531-1074) 17 (6–7), 612–620. <http://dx.doi.org/10.1089/ast.2016.1541>.
- Drumetz, L., Chanussot, J., Jutten, C., 2016. Variability of the endmembers in spectral unmixing: Recent advances. In: 2016 8th Workshop on Hyperspectral Image and Signal Processing: Evolution in Remote Sensing (WHISPERS). IEEE, Los Angeles, CA, USA, ISBN: 978-1-5090-0608-3, pp. 1–5. <http://dx.doi.org/10.1109/WHISPERS.2016.8071675>.
- Drumetz, L., Meyer, T.R., Chanussot, J., Bertozzi, A.L., Jutten, C., 2019. Hyperspectral image unmixing with endmember bundles and group sparsity inducing mixed norms. *IEEE Trans. Image Process.* (ISSN: 1941-0042) 28 (7), 3435–3450. <http://dx.doi.org/10.1109/TIP.2019.2897254>.
- Dyar, M.D., Klima, R.L., Lindsley, D., Pieters, C.M., 2007. Effects of differential recoil-free fraction on ordering and site occupancies in Mössbauer spectroscopy of orthopyroxenes. *Am. Mineral.* (ISSN: 0003-004X) 92 (2–3), 424–428. <http://dx.doi.org/10.2138/am.2007.2441>.
- Feng, Y.-Z., Sun, D.-W., 2012. Application of hyperspectral imaging in food safety inspection and control: A review. *Crit. Rev. Food Sci. Nutr.* 52 (11), 1039–1058.
- Fischer, E.M., Pieters, C.M., 1994. Remote determination of exposure degree and iron concentration of lunar soils using VIS-NIR spectroscopic methods. *Icarus* (ISSN: 0019-1035) 111, 475–488. <http://dx.doi.org/10.1006/icar.1994.1158>.
- Fleet, M.L., Bilcox, G.A., Barnett, R.L., 1980. Oriented magnetite inclusions in pyroxenes from the Grenville Province. *Can. Mineral.* 18 (1), 89–99.
- Gowen, A.A., Feng, Y., Gaston, E., Valdramidis, V., 2015. Recent applications of hyperspectral imaging in microbiology. *Talanta* 137, 43–54.
- Greenberger, R.N., Ehlmann, B.L., Osinski, G.R., Tornabene, L.L., Green, R.O., 2020. Compositional heterogeneity of impact melt rocks at the haughton impact structure, Canada: Implications for planetary processes and remote sensing. *J. Geophys. Res.: Planets* (ISSN: 2169-9100) 125 (10), <http://dx.doi.org/10.1029/2019JE006218>, e2019JE006218.
- Greenberger, R.N., Mustard, J.F., Ehlmann, B.L., Blaney, D.L., Cloutis, E.A., Wilson, J.H., Green, R.O., Fraeman, A.A., 2015. Imaging spectroscopy of geological samples and outcrops: Novel insights from microns to meters. *GSA Today : Publ. Geol. Soc. Am.* (ISSN: 1052-5173) <http://dx.doi.org/10.1130/GSATG252A.1>.
- Hapke, B., 1981. Bidirectional reflectance spectroscopy: 1. Theory. *J. Geophys. Res.: Solid Earth* 86 (B4), 3039–3054.
- Hapke, B., 1984. Bidirectional reflectance spectroscopy: 3. Correction for macroscopic roughness. *Icarus* 59 (1), 41–59.
- Hapke, B., 2012. Bidirectional reflectance spectroscopy 7: The single particle phase function hockey stick relation. *Icarus* 221 (2), 1079–1083.
- Hapke, B., Wells, E., 1981. Bidirectional reflectance spectroscopy: 2. experiments and observations. *J. Geophys. Res.: Solid Earth* 86 (B4), 3055–3060.
- Harloff, J., Arnold, G., 2001. Near-infrared reflectance spectroscopy of bulk analog materials for planetary crust. *Planet. Space Sci.* (ISSN: 0032-0633) 49 (2), 191–211. [http://dx.doi.org/10.1016/S0032-0633\(00\)00132-X](http://dx.doi.org/10.1016/S0032-0633(00)00132-X).
- Harris, J.K., Grindrod, P.M., 2018. Hapke mixture modeling applied to VNIR spectra of mafic mineral mixtures and shergottites: Implications for quantitative analysis of satellite data. *Meteorit. Planet. Sci.* (ISSN: 1945-5100) 53 (6), 1179–1206. <http://dx.doi.org/10.1111/maps.13065>.
- Heinz, D.C., Chang, C.-I., 2001. Fully constrained least squares linear spectral mixture analysis method for material quantification in hyperspectral imagery. *IEEE Trans. Geosci. Remote Sens.* 39 (3), 529–545.
- Isaacson, P.J., Klima, R.L., Sunshine, J.M., Cheek, L.C., Pieters, C.M., Hiroi, T., Dyar, M.D., Lane, M., Bishop, J., 2014. Visible to near-infrared optical properties of pure synthetic olivine across the olivine solid solution. *Am. Mineral.* (ISSN: 0003-004X) 99 (2–3), 467–478. <http://dx.doi.org/10.2138/am.2014.4580>.
- Isaacson, P.J., Sarbadhikari, A.B., Pieters, C.M., Klima, R.L., Hiroi, T., Liu, Y., Taylor, L.A., 2011. The lunar rock and mineral characterization consortium: Deconstruction and integrated mineralogical, petrologic, and spectroscopic analyses of mare basalts. *Meteorit. Planet. Sci.* (ISSN: 1945-5100) 46 (2), 228–251. <http://dx.doi.org/10.1111/j.1945-5100.2010.01148.x>.
- Johnson, J.R., 2003. Visible/near-infrared spectra of experimentally shocked plagioclase feldspars. *J. Geophys. Res.* (ISSN: 0148-0227) 108 (E11), 5120. <http://dx.doi.org/10.1029/2003JE002127>.
- Johnson, W.R., Wilson, D.W., Fink, W., M.D., M.S.H., Bearman, G.H., 2007. Snapshot hyperspectral imaging in ophthalmology. *J. Biomed. Opt.* (ISSN: 1083-3668) 12 (1), 014036. <http://dx.doi.org/10.1117/1.2434950>, 1560-2281.
- Klima, R.L., Dyar, M.D., Pieters, C.M., 2011. Near-infrared spectra of clinopyroxenes: Effects of calcium content and crystal structure. *Meteorit. Planet. Sci.* (ISSN: 1945-5100) 46 (3), 379–395. <http://dx.doi.org/10.1111/j.1945-5100.2010.01158.x>.
- Koirala, B., Zahiri, Z., Lamberti, A., Scheunders, P., 2020. Robust supervised method for nonlinear spectral unmixing accounting for endmember variability. *IEEE Trans. Geosci. Remote Sens.*
- Kokaly, R.F., Clark, R.N., Swayze, G.A., Livo, K.E., Hoefen, T.M., Pearson, N.C., Wise, R.A., Benzel, W.M., Lowers, H.A., Driscoll, R.L., 2017. USGS Spectral Library Version 7. Technical report, US Geological Survey.
- Lafuente, B., Downs, R.T., Yang, H., Stone, N., 2015. The power of databases: The RRUFF project. In: Armbruster, T., Danisi, R.M. (Eds.), *Highlights in Mineralogical Crystallography*. W. De Gruyter, Berlin, Germany, pp. 1–30.
- Leask, E.K., Ehlmann, B.L., 2016. Identifying and quantifying mineral abundance through VSWIR microimaging spectroscopy: A comparison to XRD and SEM. In: 2016 8th Workshop on Hyperspectral Image and Signal Processing: Evolution in Remote Sensing (WHISPERS). IEEE, pp. 1–5.
- Li, S., Milliken, R.E., 2015. Estimating the modal mineralogy of eucrite and diogenite meteorites using visible–near infrared reflectance spectroscopy. *Meteorit. Planet. Sci.* 50 (11), 1821–1850.
- Lu, G., Fei, B., 2014. Medical hyperspectral imaging: A review. *J. Biomed. Opt.* (ISSN: 1083-3668) 19 (1), 010901. <http://dx.doi.org/10.1117/1.JBO.19.1.010901>, 1560-2281.
- Lucey, P.G., 1998. Model near-infrared optical constants of olivine and pyroxene as a function of iron content. *J. Geophys. Res.: Planets* (ISSN: 2156-2202) 103 (E1), 1703–1713. <http://dx.doi.org/10.1029/97JE03145>.
- Mandon, L., Beck, P., Quantin-Nataf, C., Dehouck, E., Pommerol, A., Yoldi, Z., Cerubini, R., Pan, L., Martinot, M., Sautter, V., 2021. Martian meteorites reflectance and implications for rover missions. *Icarus* (ISSN: 0019-1035) 366, 114517. <http://dx.doi.org/10.1016/j.icarus.2021.114517>.
- Marty, B., Marti, K., Consortium, M., 2001. Noble gases in new SNC meteorites NWA 817 and NWA 480. *Meteorit. Planet. Sci. Suppl.* 36, A122.
- Maurice, S., Wiens, R.C., Bernardi, P., Caïs, P., Robinson, S., Nelson, T., Gasnault, O., Reess, J.-M., Deleuze, M., Rull, F., Manrique, J.-A., Abbaki, S., Anderson, R.B., André, Y., Angel, S.M., Arana, G., Battault, T., Beck, P., Benzerara, K., Bernard, S., Berthias, J.-P., Beyssac, O., Bonafous, M., Bousquet, B., Boutillier, M., Cadu, A., Castro, K., Chapron, F., Chide, B., Clark, K., Clavé, E., Clegg, S., Cloutis, E., Collin, C., Cordoba, E.C., Cousin, A., Dameury, J.-C., D’Anna, W., Daydou, Y., Debus, A., Deflores, L., Dehouck, E., Delapp, D., De Los Santos, G., Donny, C., Doressoundiram, A., Dromart, G., Dubois, B., Dufour, A., Dupieux, M., Egan, M., Ervin, J., Fabre, C., Fau, A., Fischer, W., Forni, O., Fouchet, T., Frydenvang, J., Gauffre, S., Gauthier, M., Gharakanian, V., Gilard, O., Gontijo, I., Gonzalez, R., Granena, D., Grotzinger, J., Hassen-Khodja, R., Heim, M., Hello, Y., Hervet, G., Humeau, O., Jacob, X., Jacquino, S., Johnson, J.R., Kouach, D., Lacombe, G., Lanza, N., Lapauw, L., Laserna, J., Lasue, J., Le Deit, L., Le Mouélic, S., Le Comte, E., Lee, Q.-M., Leggett, C., Leveille, R., Lewin, E., Leyrat, C., Lopez-Reyes, G., Lorenz, R., Lucero, B., Madariaga, J.M., Madsen, S., Madsen, M., Mangold, N., Manni, F., Mariscal, J.-F., Martinez-Frias, J., Mathieu, K., Mathon, R., McCabe, K.P., McConnochie, T., McLennan, S.M., Mekki, J., Melikechi, N., Meslin, P.-Y., Mischeau, Y., Michel, Y., Michel, J.M., Mimoun, D., Misra, A., Montagnac, G., Montaron, C., Montmessin, F., Moros, J., Mousset, V., Morizet, Y., Murdoch, N., Newell, R.T., Newsom, H., Nguyen Tuong, N., Ollila, A.M., Ortner, G., Oudda, L., Pares, L., Parisot, J., Parot, Y., Pérez, R., Pheav, D., Picot, L., Pilleri, P., Pilorget, C., Pinet, P., Pont, G., Poulet, F., Quantin-Nataf, C., Pictier, B., Rambaud, D., Gonzalez, R., Romano, P., Roucayrol, L., Royer, C., Ruellan, M., Sandoval, B.F., Sautter, V., Schoppers, M.J., Schröder, S., Seran, H.-C., Sharma, S.K., Sobron, P., Sodki, M., Sournac, A., Sridhar, V., Standarovskiy, D., Storms, S., Striebig, N., Tatat, M., Toplis, M., Torre-Fdez, I., Toulemont, N., Velasco, C., Veneranda, G., Venerhaus, D., Virmonitois, C., Viso, M., Willis, P., Wong, K.W., 2021. The SuperCam instrument suite on the Mars 2020 rover: Science objectives and mast-unit description. *Space Sci. Rev.* (ISSN: 1572-9672) 217 (3), 47. <http://dx.doi.org/10.1007/s11214-021-00807-w>.
- Mishchenko, M.I., Geogdzhayev, I.V., Cairns, B., Rossow, W.B., Lacić, A.A., 1999. Aerosol retrievals over the ocean by use of channels 1 and 2 AVHRR data: Sensitivity analysis and preliminary results. *Appl. Opt.* (ISSN: 2155-3165) 38 (36), 7325–7341. <http://dx.doi.org/10.1364/AO.38.007325>.
- Murchie, S.L., Mustard, J.F., Ehlmann, B.L., Milliken, R.E., Bishop, J.L., McKeown, N.K., Noe Dobrea, E.Z., Seelos, F.P., Buczkowski, D.L., Wiseman, S.M., 2009. A synthesis of Martian aqueous mineralogy after 1 Mars year of observations from the Mars Reconnaissance Orbiter. *J. Geophys. Res.: Planets* 114 (E2).
- Mustard, J.F., Pieters, C.M., 1989. Photometric phase functions of common geologic minerals and applications to quantitative analysis of mineral mixture reflectance spectra. *J. Geophys. Res.: Solid Earth* 94 (B10), 13619–13634.
- Pieters, C.M., 1983. Strength of mineral absorption features in the transmitted component of near-infrared reflected light: First results from RELAB. *J. Geophys. Res.: Solid Earth* (ISSN: 2156-2202) 88 (B11), 9534–9544. <http://dx.doi.org/10.1029/JB088iB11p09534>.

- Pompilio, L., Sgavetti, M., Pedrazzi, G., 2007. Visible and near-infrared reflectance spectroscopy of pyroxene-bearing rocks: New constraints for understanding planetary surface compositions. *J. Geophys. Res.: Planets* (ISSN: 2156-2202) 112 (E1), <http://dx.doi.org/10.1029/2006JE002737>.
- Roedder, E., 1965. Liquid CO₂ inclusions in olivine-bearing nodules and phenocrysts from Basalts 1. *Am. Mineral.* (ISSN: 0003-004X) 50 (10), 1746–1782.
- Scowen, P.A.H., Roeder, P.L., Helz, R.T., 1991. Re-equilibration of chromite within Kilauea Iki Lava Lake, Hawaii. *Contrib. Mineral. Petrol.* (ISSN: 1432-0967) 107 (1), 8–20. <http://dx.doi.org/10.1007/BF00311181>.
- Serventi, G., Carli, C., Sgavetti, M., Ciarniello, M., Capaccioni, F., Pedrazzi, G., 2013. Spectral variability of plagioclase–mafic mixtures (1): Effects of chemistry and modal abundance in reflectance spectra of rocks and mineral mixtures. *Icarus* 226 (1), 282–298.
- Shkuratov, Y., Starukhina, L., Hoffmann, H., Arnold, G., 1999. A model of spectral albedo of particulate surfaces: Implications for optical properties of the Moon. *Icarus* 137 (2), 235–246.
- Sunshine, J.M., Pieters, C.M., Pratt, S.F., McNaron-Brown, K.S., 1999. Absorption band modeling in reflectance spectra: Availability of the modified Gaussian model. *LPI* 1306.
- Tait, S., 1992. Selective preservation of melt inclusions in igneous phenocrysts. *Am. Mineral.* (ISSN: 0003-004X) 77 (1–2), 146–155.
- Tatzer, P., Wolf, M., Panner, T., 2005. Industrial application for inline material sorting using hyperspectral imaging in the NIR range. *Real-Time Imaging* 11 (2), 99–107.
- Tompkins, S., Pieters, C.M., 1999. Mineralogy of the lunar crust: Results from Clementine. *Meteorit. Planet. Sci.* (ISSN: 1945-5100) 34 (1), 25–41. <http://dx.doi.org/10.1111/j.1945-5100.1999.tb01729.x>.
- Vo-Dinh, T., 2004. A hyperspectral imaging system for in vivo optical diagnostics. *IEEE Eng. Med. Biol. Mag.* (ISSN: 1937-4186) 23 (5), 40–49. <http://dx.doi.org/10.1109/MEMB.2004.1360407>.
- Wan, X., Yuan, R., Wang, H., Cheng, Y., Jia, J., Shu, R., Xu, W., Li, C., Xin, Y., Ma, H., Fang, P., Ling, Z., 2021. Elastic particle swarm optimization for MarSCoDe spectral calibration on Tianwen-1 Mars rover. *Anal. Chem.* (ISSN: 0003-2700) 93 (22), 7970–7977. <http://dx.doi.org/10.1021/acs.analchem.1c00832>.
- Wang, L., Moon, N., Zhang, Y., Dunham, W.R., Essene, E.J., 2005. Fe-Mg order-disorder in orthopyroxenes. *Geochim. Cosmochim. Acta* (ISSN: 0016-7037) 69 (24), 5777–5788. <http://dx.doi.org/10.1016/j.gca.2005.08.011>.
- Wiens, R.C., Maurice, S., Robinson, S.H., Nelson, A.E., Cais, P., Bernardi, P., Newell, R.T., Clegg, S., Sharma, S.K., Storms, S., Deming, J., Beckman, D., Ollila, A.M., Gasnault, O., Anderson, R.B., André, Y., Michael Angel, S., Arana, G., Auden, E., Beck, P., Becker, J., Benzerara, K., Bernard, S., Beyssac, O., Borges, L., Bousquet, B., Boyd, K., Caffrey, M., Carlson, J., Castro, K., Celis, J., Chide, B., Clark, K., Cloutis, E., Cordoba, E.C., Cousin, A., Dale, M., Deflores, L., Delapp, D., Deleuze, M., Dirmyer, M., Donny, C., Dromart, G., George Duran, M., Egan, M., Ervin, J., Fabre, C., Fau, A., Fischer, W., Forni, O., Fouchet, T., Fresquez, R., Frydenvang, J., Gasway, D., Gontijo, I., Grotzinger, J., Jacob, X., Jacquiod, S., Johnson, J.R., Klisiewicz, R.A., Lake, J., Lanza, N., Laserna, J., Lasue, J., Le Mouélic, S., Legett, C., Leveille, R., Lewin, E., Lopez-Reyes, G., Lorenz, R., Lorigny, E., Love, S.P., Lucero, B., Madariaga, J.M., Madsen, M., Madsen, S., Mangold, N., Manrique, J.A., Martinez, J.P., Martinez-Frias, J., McCabe, K.P., McConnochie, T.H., McGlown, J.M., McLennan, S.M., Melikechi, N., Meslin, P.-Y., Michel, J.M., Mimoun, D., Misra, A., Montagnac, G., Montmessin, F., Mousset, V., Murdoch, N., Newsom, H., Ott, L.A., Ousnamer, Z.R., Pares, L., Parot, Y., Pawluczuk, R., Glen Peterson, C., Pilleri, P., Pinet, P., Pont, G., Poulet, F., Provost, C., Quertier, B., Quinn, H., Rapin, W., Reess, J.-M., Regan, A.H., Reyes-Nowell, A.L., Romano, P.J., Royer, C., Rull, F., Sandoval, B., Sarrao, J.H., Sautter, V., Schoppers, M.J., Schröder, S., Seitz, D., Shepherd, T., Sobron, P., Dubois, B., Sridhar, V., Toplis, M.J., Torre-Fdez, I., Trettel, I.A., Underwood, M., Valdez, A., Valdez, J., Venhaus, D., Willis, P., 2020. The SuperCam instrument suite on the NASA Mars 2020 rover: Body unit and combined system tests. *Space Sci. Rev.* (ISSN: 1572-9672) 217 (1), 4. <http://dx.doi.org/10.1007/s11214-020-00777-5>.
- Winter, M.E., 1999. N-FINDR: An algorithm for fast autonomous spectral end-member determination in hyperspectral data. In: *Imaging Spectrometry V*, Vol. 3753. *International Society for Optics and Photonics*, pp. 266–275.
- Yang, Y., Li, S., Milliken, R.E., Zhang, H., Robertson, K., Hiroi, T., 2019. Phase functions of typical lunar surface minerals derived for the Hapke model and implications for visible to near-infrared spectral unmixing. *J. Geophys. Res.: Planets* (ISSN: 2169-9100) 124 (1), 31–60. <http://dx.doi.org/10.1029/2018JE005713>.
- Zhang, H., Yang, Y., Jin, W., Liu, C., Hsu, W., 2014. Effects of Spectralon absorption on reflectance spectra of typical planetary surface analog materials. *Opt. Express* (ISSN: 1094-4087) 22 (18), 21280–21291. <http://dx.doi.org/10.1364/OE.22.021280>.